A Self-amplified Near-infrared Bipolar Phototransistor with a PbSe Nanoband Array Heterostructure for Pharmaceutical Solute Detection

Yujie Fu[1], Chun Lei[1], Long Teng[1], Yongbing Zhu[1,3], Liyao Jiang[1], Yuqin Cai[1], Dandan Zhou[2], Zhi Tao[1*]

Abstract—**This paper introduces a new device concept and outlines the fabrication process of a bipolar junction transistor based on an IGZO/NiO/PbSe nanoband array heterostructure. We performed comprehensive electrical property testing and characterization analysis on the device to thoroughly assess the device's performance. The heterojunction structure efficiently amplifies the opto-electric responsivity and enhances the transmission efficiency of photogenerated carriers. Significantly, the phototransistor demonstrates a high photoresponsivity of 4000 A/W under an incident light power of 1 μW/cm² and a wavelength of 850 nm. Hence, a solution detection system integrated with a bipolar phototransistor is designed. Through the analysis of the output signals, the system accurately determines the identity of the solute present in the solution.**

Index Terms—**Phototransistor, heterojunction, bipolar junction transistor (BJT), PbSe nanoband**

I. INTRODUCTION

TO DATE, infrared photoelectric detection has garnered significant attention from scientific researchers due to its wide application in aerospace remote sensing, military equipment, earth imaging and gas monitoring [1]. Photodetectors offer remarkable advantages, including rapid response, high sensitivity, and wavelength selectivity [1]. Furthermore, attributes such as high gain and low noise are important considerations driving the study of photodetectors (PDs) [2]. In the field of medical diagnosis, photodetectors also play an important role. Beyond infrared imaging, their applications extend to solution detection, illustrating their broad relevance and utility. Spectral analysis serves as the primary method for analyzing the composition of solutions. The integration of photodetectors and electronic devices enables abundant interactions between substances, thus requiring a fast response and reliable photodetector arrays [3].

Indium gallium zinc oxide (IGZO), a fourth-generation semiconductor material, stands out as a thin-film transistor (TFT) technology capable of serving as a wide-band gap channel material for high-performance TFTs. Moreover, IGZO has high electron mobility [4]. Most nickel oxide studies predominantly focus on electrochromics, hole transport, and gas-sensitive sensors [5]. Nevertheless, there is still a scarcity of reports on photoelectric detection, leaving ample room for further exploration of nickel oxide (NiO). Due to its intrinsic p-type semiconductor material properties, NiO possesses a wide bandgap of approximately 3.6 eV, high chemical stability and compatibility at low processing temperatures [6]. The high hole mobility of NiO markedly helps in the generation of photocurrent [7]. Another n-type material chosen for this study is PbSe quantum dots. Compared with the previous two semiconductor materials, PbSe has a narrow band gap of approximately 0.28 eV. PbSe nanomaterials from IV-VI compounds have characteristics such as a high modulation bandwidth, low Auger coefficient, and large excitation Bohr radius and have attracted much attention due to their appropriate energy band structure and excellent ability to absorb light [8], enhancing the performance of two-dimensional photodetectors. Consequently, PbSe has wide application prospects in near-infrared optoelectronic devices and widespread use in lasers, light-emitting diodes, photovoltaic devices, and photodetectors [9].

Photodiodes are diffusely utilized optoelectronic devices that are renowned for their sensitivity to light signals and fast response, making them ideal for detecting swiftly changing optical signals [10]. However, its limitations include a small photosensitive area and lack of internal gain. Photo-detectors leveraging field-effect transistors mitigate this drawback by utilizing gate voltage to enhance optical gain, separating photogenerated carriers and achieving heightened sensitivity [11]. Conversely, a photodetector employing a bipolar junction transistor (BJT) structure could offer superior internal gain, allowing operation at a lower bias voltage. Additionally, the photocurrent remains relatively stable even with changes in the base-collector voltage when the transistor operates in the amplification region. This inherent stability significantly bolsters system reliability, even under voltage fluctuations or disturbances. [2].

Photodetectors featuring heterogeneous structures exhibit great responsiveness, facilitating more effective conversion of optical signals into current signals [12]. Heterojunction phototransistors (PTs) represent a category of photodetectors known for their capacity to deliver high optical gain while operating at low bias voltages [13]. Consequently, it makes sense to investigate heterojunctions for high-sensitivity photodetectors.

In this paper, a high-performance IGZO/NiO/PbSe nanoband-array (NA) bipolar junction transistor was reported for the manufacturing of this device. The experimental data indicate that the BJT based on IGZO/NiO/PbSe(NA) demonstrates significant efficiency with a responsivity of 4000 A/W. The device's low photoelectric noise and high optical gain hold profound potential for a wide range of innovative applications. With STM32 carrying out analog-to-digital conversion and subsequently transmitting the resulting data to the computer for analysis, the specially designed detection circuit with the NPN PT demonstrates accurate solute detection within the solution.

II. MATERIAL AND DEVICE PREPARATION

The glass substrate was sequentially cleaned for 10 minutes each using acetone, ethanol and deionized water. A four-terminal heterojunction BJT phototransistor was fabricated on an electronic-grade glass substrate. The silver gate electrode was printed on glass substrates using an EHDjet-H with a 5-micron needle, followed by thermal annealing at 150 °C for 30 minutes. Subsequently, the insulating material ink LOGI-DT15A was spin-coated onto the glass substrate at 2000 rpm for one minute. Following the spin-coating process, the device underwent thermal treatment at 150 °C for half an hour. The emitter was then printed onto the insulating layer material using an electrofluid inkjet printer and subjected to thermal annealing. Next, the IGZO and NiO materials were deposited onto a glass substrate via magnetron sputtering with base electrode printing and subsequently annealed. Using laser etching techniques, PbSe thin films were selectively etched with a laser power of 262 mJ/cm^2 and a wavelength of 560 nm. This process yielded a PbSe nanoband array characterized by a gap width of 150 nm and a width of 60 nm while preserving the integrity of the NiO layer. The PbSe nanoband array could be observed via SEM, as illustrated in Figure 1a.

Compared with the thin-film structure, the nanoband array produced in the experiment demonstrated enhanced responsiveness to near-infrared wavelengths. This observation is further supported by the data presented in Figure 1b.
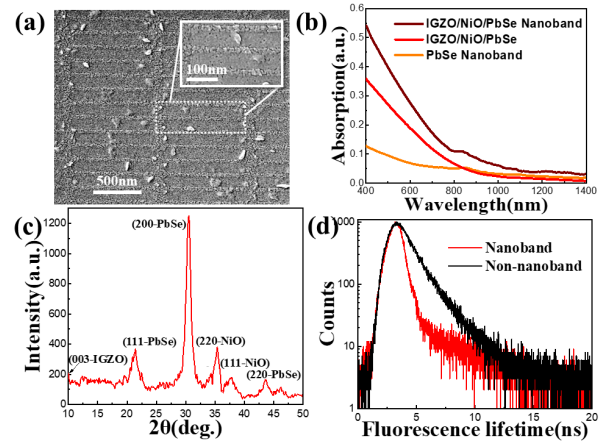

Fig. 1. (a) SEM image of the phototransistor. **(b)** Absorption spectroscopy of the IGZO/NiO/PbSe device. **(c)** XRD image of the IGZO/NiO/PbSe NPN phototransistor. **(d)** Fluorescence lifetime curves measured for the nanoband structure and the non-nanoband structure.

Figure 1c displays the X-ray diffraction (XRD) pattern of the transistor material IGZO/NiO/PbSe, revealing a prominent diffraction peak occurring at approximately 30°. Fluorescence lifetime curves are depicted for transistors featuring both PbSe nanobands and non-nanobands, as illustrated in Figure 1d. The IGZO/NiO/PbSe BJT transistors with PbSe nanobands have shorter carrier lifetimes than those without PbSe nanobands. This is because IGZO and PbSe are both n-type materials, while NiO is a p-type material. These materials serve as electron and hole transport materials, respectively, which is advantageous for fabricating high-performance optoelectronic transistors.

III. RESULTS AND DISCUSSION

We systematically investigated the electrical characteristics of the BJT to assess its performance.

Two types of devices were manufactured, namely, nanoband and non-nanoband structures, as demonstrated in Figure 2a and Figure 2b, respectively, to assess the electrical properties of the device. Figure 2c shows the input characteristic curve of the common-base configuration, where the voltage between the collector and the base remains constant, while the emitter current increases with increasing voltage between the base and the emitter. Notably, the emitter current increases with increasing V_{CB}, while the V_{BE} remains constant. Figure 2d and Figure 2f show the output characteristic curves of the common-base and common-emitter configurations of the triodes, showing similar regularity to the input characteristic curve. The common-emitter curve resembles the common-base characteristic curve. However, a notable difference emerges. When V_{BE} remains constant in the input characteristic curve, the base current decreases as V_{CE} increases, as shown in Figure 2e. These obtained characteristic curves furnish adequate data for calculating the two gains of the two configurations.
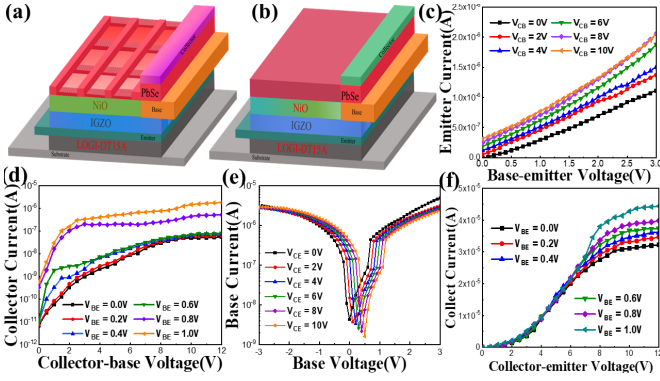
Fig. 2. (a, b) Schematics of the compared nanoband and non-nanoband phototransistor structures. **(c)** I_E-V_{BE} curves of devices with various V_{CB} voltages. **(d)** I_C-V_{CB} curves of devices with various V_{BE} voltages. **(e)** I_B-V_{BE} curves of devices with various V_{CE} voltages. **(f)** I_C-V_{CE} curves of devices with various V_{BE} voltages.

As stated previously, we have undertaken a comprehensive analysis of the gain in both the common-base and common-emitter configurations of the device. The two gains can be calculated using Equation (1) and Equation (2) [14], [15].

$$\alpha = \frac{I_C}{I_E} \qquad (1)$$

$$\beta = \frac{I_C}{I_B} \qquad (2)$$

In the aforementioned formula, I_C represents the collector current, I_E denotes the emitter current, and I_B indicates the base current. Through the calculation of the gain, depicted in Figure 3a, the gain of the common-base configuration improves with increasing input current. Conversely, as illustrated in Figure 3b, the gain of the common-emitter configuration decreases as the input current increases.
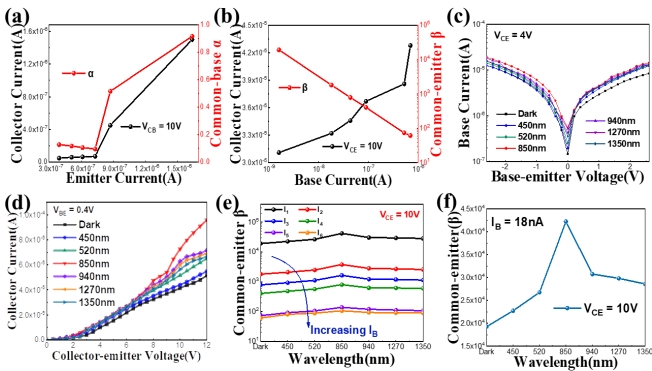

Fig. 3. (a) α-I_E for a common-base amplifier circuit (V_{CB}=10 V). **(b)** β-I_B for the common-emitter amplifier circuit (V_{CE}=10 V). **(c)** I_B-V_{BE} curve for the device at various wavelengths (input characteristic curve of the common emitter). **(d)** I_C-V_{CE} curve for the device at different wavelengths (output characteristic curve of the common emitter). **(e)** β-Wavelength curve for the

device under different input currents. **(f)** β-Wavelength curve for the device at an input current of 18 nA (V_{CE}=10 V).

Following electrical tests conducted on the devices without illumination, we tested the electrical characteristic curves of the devices in the common-emitter configuration under various light wavelengths. As depicted in Figure 3c, the input current increases as the incident light transitions from lower to higher wavelengths. However, a notable deviation occurs once the incident light wavelength reaches 850 nm. The input current begins to decrease gradually, as illustrated in Figure 3c. This observed trend persists in the output characteristic curve, as demonstrated in Figure 3d. The common-emitter gain under illumination, computed using Equation (2), is presented in Figure 3e. It is evident that the common-emitter gain increases with increasing incident light wavelength until reaching 850 nm, after which it decreases. Moreover, the gain diminishes as the input current increases from I1 to I6 under a constant incident light wavelength. Employing a base current of 18 nA as the standard operational state and maintaining the V_{CE} at 10 V, the gain reaches a magnitude of four as the incident light wavelength shifts to higher bands. The peak at 850 nm subsequently decreases, as depicted in Figure 3f. According to Figure 3f, the photogain of the phototransistor reaches 4.22×10^4 at 850 nm.

The experimental results show that the device works optimally at a wavelength of 850 nm.

The channel area can be estimated to be 100 μm×40 μm. With an incident power intensity of 1 μW/cm², the photoresponsivity is accurately calculated, and the output characteristic curve of the common-emitter circuit is presented in Figure 3d. The photoresponsivity can be determined using Equation (3) [16].

$$R = \frac{I_{\text{total}} - I_{\text{dark}}}{P} = \frac{I_{ph}}{\rho \cdot S} \qquad (3)$$

In the above equation, P represents the optical power, I_{total} is the total current, I_{dark} is the dark current, I_{ph} is the photocurrent, ρ is the optical incident power density, and S is the effective area of the photoelectric reaction. Investigating the responsivity across different incident light wavelengths, as depicted in Figure 4e, reveals a progressive increase in the responsivity from 750 A/W to 4000 A/W with increasing incident light wavelength. Moreover, as shown in Figure 4e, the external quantum efficiency (EQE) increased from 827.5% to 2336.5%. The EQE can be calculated using Equation (4).

$$EQE = \frac{I_{ph} / q}{\rho / h\nu} \times 100\% \qquad (4)$$

The flicker noise in a MOSFET device arises from the stochastic capture and release of carriers by the interface trap energy state [17]. The response frequency of a photodetector is intricately linked to the carrier transfer efficiency induced by light, which may be affected by noise. In the case of the BJT device, the dominant sources of noise include base resistance thermal noise and collector current shot noise [18]. However,

in comparison to MOSFETs, BJTs exhibit lower levels of flicker noise owing to their bulk conduction mechanism [17]. This performance enhances the carrier transmission efficiency, impacting the frequency response of the photodetector.
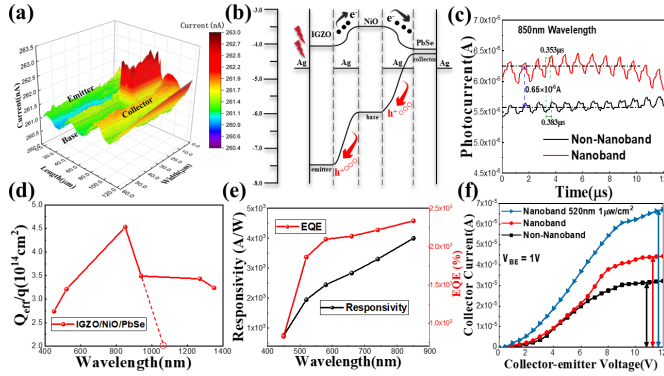

Fig. 4. (a) The measured position-dependent photocurrent for the nanoband structure phototransistor channel. **(b)** Energy band and charge transfer diagrams of the heterostructure structure device. **(c)** Light signal response comparison for the nanoband structure and the non-nanoband structure (850 nm and 1 μW/cm²). **(d)** Efficient photogenerated carrier density stored in the phototransistors at various wavelengths. **(e)** Responsivity and EQE at different wavelengths. **(f)** Current under the nanoband and non-nanoband structures (V_BE=1 V).

Bipolar junction transistors, as fundamental transistors, are distinguished by their high transconductance and output resistance, making them crucial in the design of high-frequency circuits. Their versatility stands out because they could serve as ideal amplifiers or switches in such circuitry applications [19].

Within the semiconductor heterostructure, the intermediate layer possesses a lower energy band, facilitating the efficient injection of electrons from adjacent layers. This phenomenon augments the current flow from the collector to the emitter in the transistor, consequently enhancing the amplification factor of the transistor. Moreover, decreasing the thickness of the base region and augmenting the doping concentration within it can further enhance the reaction rate of the device. Consequently, heterostructures are instrumental in the fabrication of rapid-response transistors.

Recently, extensive research efforts have been dedicated to exploring two-dimensional semiconductors, emphasizing their high responsivity, elevated detection rate, and low power consumption. Owing to their minute scale, long photoelectronic lifetime, tunable light absorption characteristics and heightened carrier mobility, low-dimensional nanomaterials have excellent optoelectronic properties, including high response rates, fast response and low power consumption [20].

Studying the photoelectric response at the corresponding position of the phototransistor is highly important for further understanding the photoelectric response characteristics of the transistor. Figure 4a illustrates the position- and spectrally dependent photocurrent mapping conducted to analyze and characterize the static optoelectronic performance of the designed device. Under the illumination of the heterojunction structure, the area encompassing the base region exhibits an elevated photoresponse, while a decrease in photoresponse is observed toward the channel. This indicates that under biased and heterostructured conditions, an enhanced photoresponse can be achieved.

An energy band schematic diagram of the BJT device is depicted in Figure 4b, showing that carrier transfer occurs at the IGZO/NiO and NiO/PbSe interfaces. IGZO exhibits remarkable optical properties, facilitating the generation of electron-hole pairs in the emitter region upon exposure to incident light under an appropriate bias voltage [21]. Carriers generated by irradiation undergo transport between the emitter junction and the collector junction. Electrons migrate from the emitter to the base via drift motion, while a portion of these electrons recombine with holes within the base region, giving rise to the base current. Simultaneously, the bias voltage applied to the collector junction maintains a reverse state, ensuring that electrons drifting toward the base region are efficiently collected by the collector, thereby contributing to the formation of the collector current [21]. The BJT device, which is endowed with heterojunction structures, effectively mitigates photoelectric noise while enhancing photoelectric conversion efficiency.

$$I_C = -A\left[\frac{qD_{nb}n_{b0}}{W_b}\left(\exp\left(\frac{qV_{BE}}{KT}\right)-1\right)-\left(\frac{qD_{nb}n_{b0}}{W_b}+\frac{qD_{pe}P_{c0}}{L_{pc}}\right)\left(\exp\left(\frac{qV_{BC}}{KT}\right)-1\right)\right]$$

(5)

A is the junction area of the emitter junction and collector junction. W_b refers to the effective width of the base region. L_{PC} denotes the diffusion length of minority carriers (holes) in the collector region. D_{nb} and D_{pe} represent the diffusion coefficients of minority carriers (electrons) in the base region and minority carriers (holes) in the collector area, respectively. n_{b0} signifies the nonequilibrium minority carrier concentration in the base area. P_{c0} is the nonequilibrium minority carrier concentration in the collector region.

Bipolar junction transistors constitute a crucial component of integrated circuits. The PNP BJT configuration consists of two back-to-back PN junctions [22]. The NPN BJT exhibited a similar structure. From Equation (5) above, according to Figure 4f, the current is greater for the nanoband structure than for the non-nanoband structure. When V_{BE} is 1 V, the collector current of the device approaches 70 μA when exposed to incident light at 520 nm and 1 μW/cm². Compared with the non-nanoband device, the nanoband device has a greater current under identical conditions, suggesting a lower defect density and enhanced responsiveness to incident light. The PbSe nanoband features a rectangular cross-section, showing well-defined shapes and high crystallinity. When utilized in the fabrication of nanostructured photodetectors, the morphology and crystallinity of the nanobands augment device sensitivity and response speed [23]. The high surface area of the nanobands suggests an increased number of active sites, thereby enhancing

interfacial interactions [24]. The crystalline characteristics of nanobands reflect the ordered arrangement of atoms within the nanoband structure, resulting in a lower defect density. This characteristic increase in the ordered arrangement enhances the electron transport properties within the nanobands, consequently improving the response speed of the photodetectors. In addition, the nanoband structure effectively shortens electron transport paths and facilitates efficient current injection, improving charge carrier transport rates [25]. The utilization of this nanoband structure has led to favorable outcomes in photodetectors.

Moreover, research on stored effective charges elucidates the densities of photoexcited effective charges [26].

$$\Delta Q_{\text{eff}}(\varepsilon) = C_{ox} \cdot \Delta V_{th}(\varepsilon) \tag{6}$$

When exposed to incident light of various wavelengths, the IGZO/NiO/PbSe(NA) device demonstrates remarkable photocarrier storage capabilities, reaching up to 14 orders of magnitude. As illustrated in Figure 4d, little ΔV_{th} absorption was observed below a wavelength of 1070 nm, which indicated a low trap density within the experimental setup.

The broadband detection characteristics promote the photogeneration of electrons and holes near the n-IGZO/p-NiO heterojunction [27]. The measurement was conducted under a constant emitter-collector voltage of 10 V [28]. The photoresponse time is influenced by both the photocarrier injection mechanism and lattice matching. With each additional 1 V increase in the base voltage, the corresponding increase in the photoresponse current is calculated. Figure 4c shows an approximate 6.25 μA photocurrent with the nanoband structure, while the photocurrent is approximately 5.6 μA with the non-nanoband structure. Holes, which are generated by light irradiation, accumulate in the base region, consequently inducing more electron current from the emitter, amplifying the photocurrent [27].

To assess the detectivity of this device for comparison, it is crucial to understand that the detectivity (D*) represents the sensor's ability to detect even the faintest optical signal [29], particularly in dynamic detection scenarios. It quantifies the relationship between the sensor and its inherent noise, a correlation that can be confirmed through the demonstration of the noise current spectrum. The following formula outlines the calculation of the detectivity [30]:

$$NEP = \frac{I_N}{R}\left(wHz^{-\frac{1}{2}}\right) \tag{7}$$

$$D^* = \frac{\sqrt{A}}{NEP}\left(cmHz^{\frac{1}{2}}/w, \text{ Jones}\right) \tag{8}$$

In the two equations above, NEP is the noise equivalent power, I_N is the noise current density, A is the active area, and R is the responsivity.

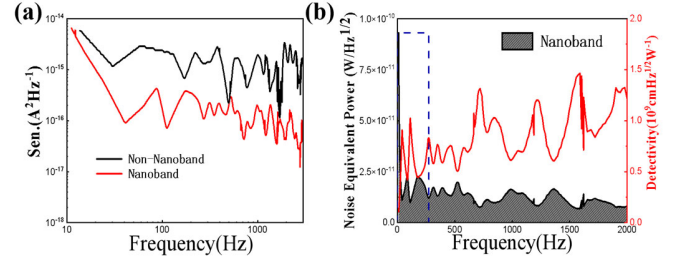$$\int_0^\infty NEP(f)d(f) = NEP(f)\Delta(f) \tag{9}$$

Fig. 5. (a, b) The ameliorative NPN phototransistor's noise equivalent power (NEP) and detectivity spectrum related to the base frequency under a dynamic detection environment.

As illustrated in Figure 5a, the NPN PT maintains a lower noise current density due to its lower noise current and nanoband structure. Figure 5b shows the dynamic performance of the NPN PT.

The experimental results indicate a modulation bandwidth of 2000 Hz, underscoring the substantial influence of the contact interface in the channel, which significantly affects the device's behavior and performance. Simultaneously, the detectivity of the NPN PT can reach 1.25×10^9 Jones synchronously in dynamic detection scenarios.

TABLE I
COMPARISON OF THIS STUDY WITH OTHER PHOTO-
TRANSISTORS DESCRIBED IN THE LITERATURE

Materials	Responsivity (A/W)	EQE (%)	Photogain	Reference
IGZO/NiO/PbSe	4×10^3	2336.5	4.22×10^4	This work
C8-BTBT/MAPbBr₃/C8-BTBT	1.28	500	600	[31]
WSe₂/SnSe₂/WSe₂	65	26	21.2	[32]
IGZO/SnO₂	328.6	~	~	[33]
4H-SiC	125	~	1450	[34]

Compared to the currently published phototransistors listed in TABLE I, our proposed NPN heterojunction phototransistor exhibits excellent responsivity, EQE, and photodetectivity. These results indicate the significant potential of this device for future phototransistor applications.

Triode photodetectors continue to hold significant potential for many fields [32]. Figure 6a shows a schematic diagram outlining the framework of NPN PT in solution detection.

A distributed feedback (DFB) laser is a laser capable of regulating light wavelength [36]. A signal generator produces a sawtooth wave scanning signal, superimposing a modulation signal of fast sinusoidal frequency f on the laser driver to drive the DFB laser. Consequently, the laser outputs two channels of modulated light, which are utilized to vertically illuminate the two solution bags, with one serving as the reference object. The

NPN PT array detects and converts the absorbed light intensities into optical signals, which are subsequently transformed into current signals. The two current signals are then converted into two voltage signals through the current-voltage module (ADA4530) and further amplified via an operational amplifier (OP07). STM32 processes and transmits the data to a computer through a differential amplification circuit and demodulation process.
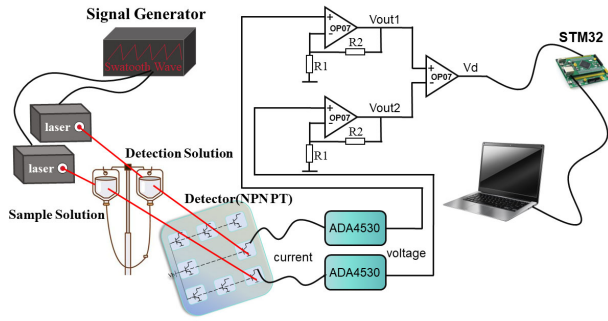

Fig. 6. a Framework diagram of the heterojunctions of NPN PT in solution detection.

Chemical bonds, particularly carbon–hydrogen bonds within semiconductor materials, exhibit vibrations that couple with light vibrations, resulting in light absorption phenomena. This absorption, which is induced by molecular vibrations, serves as an important tool for analyzing substance composition and concentration [37], [38]. Observably, strong absorption occurs within the 1064 nm wavelength band at frequencies exceeding 1 MHz. The intensity of light absorption proportionally increases as the frequency increases. Biapenem presented a downward peak, while ambroxol hydrochloride displayed an upward peak. Figure 7a and Figure 7c show that the trough of 0.1 g/100 ml biapenem in sodium chloride is significantly smaller than that in sodium chloride. Furthermore, Figure 7a and 7b illustrates the difference in biapenem concentrations within the same glucose solution at 500 kHz. These findings underscore the precision of our device in discerning both the type and concentration of various solutes.
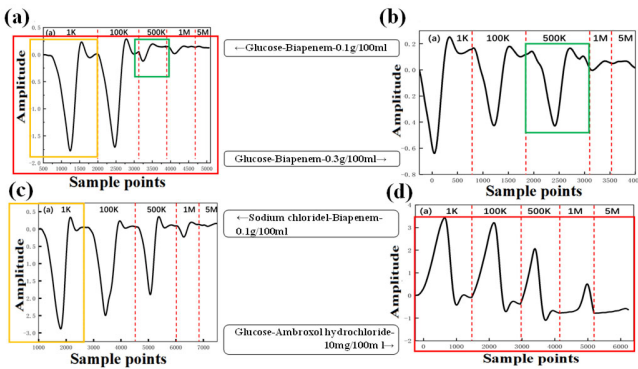

Fig. 7. (a, b) Absorption reflected by the detection signal amplitudes of glucose-biapenem at various concentrations. **(c,**

d) The signal detection amplitudes of sodium chloride biapenem and glucose-ambroxol hydrochloride.

IV. CONCLUSION

In conclusion, the IGZO/NiO/PbSe heterojunction with the PbSe nanoband phototransistor fabricated in this research exhibits good photoelectric properties, rendering it suitable for high-performance bipolar phototransistors. Notably, the device achieved a remarkable photoresponsivity of 4000 A/W at 850 nm, accompanied by an EQE of 2336.5%. Leveraging its heterojunction structure, the device achieves a maximal photogain of 4.22×10^4 at 10 V and 850 nm. The device's low noise and defect density substantially enhance its transmission efficiency, improving the phototransistor's performance. Moreover, the experimental results reveal the potential of applying NPN PT in applications requiring superior response rates, gains, and detectivity. When integrated into a circuit, the NPN transistor contributed to the development of an integrated solution detection system capable of accurately discerning solutes within diverse solutions.

REFERENCES

[1] T. Murata, S. Asahi, S. Sanguinetti, and T. Kita, "Infrared photodetector sensitized by InAs quantum dots embedded near an Al0.3Ga0.7As/GaAs heterointerface," *Sci Rep*, vol. 10, no. 1, p. 11628, Jul. 2020, doi: 10.1038/s41598-020-68461-w.

[2] C. Sun *et al.*, "Bidirectional Bias Response Ultraviolet Phototransistors With 4H-SiC NPN Multi-Layer Structure," *IEEE Photon. Technol. Lett.*, vol. 34, no. 2, pp. 81–84, Jan. 2022, doi: 10.1109/LPT.2021.3140075.

[3] X. Han, W. Du, R. Yu, C. Pan, and Z. L. Wang, "Piezo-Phototronic Enhanced UV Sensing Based on a Nanowire Photodetector Array," *Advanced Materials*, vol. 27, no. 48, pp. 7963–7969, Dec. 2015, doi: 10.1002/adma.201502579.

[4] T.-C. Lin, W.-C. Huang, and W.-C. Lan, "A study on the electrical and optical characteristics of IGZO films," *J Mater Sci: Mater Electron*, vol. 25, no. 7, pp. 3077–3084, Jul. 2014, doi: 10.1007/s10854-014-1986-z.

[5] X. Deng, L. Zhang, J. Guo, Q. Chen, and J. Ma, "ZnO enhanced NiO-based gas sensors towards ethanol," *Materials Research Bulletin*, vol. 90, pp. 170–174, Jun. 2017, doi: 10.1016/j.materresbull.2017.02.040.

[6] Y.-R. Li *et al.*, "Sensitivity Enhancement of Ultraviolet Photodetectors With the Structure of p-NiO/Insulator-SiO $_2$ /n-ZnO Nanowires," *IEEE Electron Device Lett.*, vol. 36, no. 8, pp. 850–852, Aug. 2015, doi: 10.1109/LED.2015.2448721.

[7] M. Ding *et al.*, "Self-Powered p-NiO/n-Ga $_2$ O $_3$ Heterojunction Solar-Blind Photodetector With Record Detectivity and Open Circuit Voltage," *IEEE Electron Device Lett.*, vol. 44, no. 2, pp. 277–280, Feb. 2023, doi: 10.1109/LED.2022.3227583.

[8] L. Yun, L. Zhu, X. Liu, F. Ye, and Z. Zhang, "Low Threshold and High Power Fiber Laser Passively Mode-Locked Based on PbSe Quantum Dots," *IEEE Photon. Technol. Lett.*, vol. 36, no. 4, pp. 247–250, Feb. 2024, doi: 10.1109/LPT.2024.3349468.

[9] Yang D. *et al.*, "Research Progress in Surface Modification Engineering and Application of PbSe Quantum Dots," *Laser Optoelectron. Prog.*, vol. 60, no. 15, p. 1500004, 2023, doi: 10.3788/LOP221857.

[10] A. M. Selman, Z. Hassan, M. Husham, and N. M. Ahmed, "A high-sensitivity, fast-response, rapid-recovery p–n heterojunction photodiode based on rutile TiO2 nanorod array on p-Si(111)," *Applied Surface Science*, vol. 305, pp. 445–452, Jun. 2014, doi: 10.1016/j.apsusc.2014.03.109.

[11] D. Yang *et al.*, "Pentacene-Based Photodetector in Visible Region With Vertical Field-Effect Transistor Configuration," *IEEE Photon. Technol. Lett.*, vol. 27, no. 3, pp. 233–236, Feb. 2015, doi: 10.1109/LPT.2014.2365498.

[12] Y. Meng *et al.*, "A Novel PbS/n-IGZO Thin-Film Nano-Photodetector with High Responsivity and High Photo-to-Dark Current Ratio," in *2018 IEEE 13th Annual International Conference on Nano/Micro Engineered and Molecular Systems (NEMS)*, Singapore: IEEE, Apr. 2018, pp. 131–134. doi: 10.1109/NEMS.2018.8557018.

[13] Z. Liao, Z. Lv, and H. Jiang, "InGaN Visible Light Heterojunction Phototransistor," in *Asia Communications and Photonics Conference/International Conference on Information Photonics and Optical Communications 2020 (ACP/IPOC)*, Beijing: Optica Publishing Group, 2020, p. M4A.26. doi: 10.1364/ACPC.2020.M4A.26.

[14] G. Dastgeer, Z. M. Shahzad, H. Chae, Y. H. Kim, B. M. Ko, and J. Eom, "Bipolar Junction Transistor Exhibiting Excellent Output Characteristics with a Prompt Response against the Selective Protein," *Adv Funct Materials*, vol. 32, no. 38, p. 2204781, Sep. 2022, doi: 10.1002/adfm.202204781.

[15] J. Zhang, X. Li, P. Alexandrov, L. Fursin, X. Wang, and J. H. Zhao, "Fabrication and Characterization of High-Current-Gain 4H-SiC Bipolar Junction Transistors," *IEEE Trans. Electron Devices*, vol. 55, no. 8, pp. 1899–1906, Aug. 2008, doi: 10.1109/TED.2008.926670.

[16] Y. Liu, L. Yuan, C. Sun, Y. Zhang, X. Tang, and Y. Zhang, "Three-Dimensional Design of a 4H-SiC NPN Lateral Phototransistor for Micro-Pixel in Ultraviolet Optoelectronic Integration," *IEEE Trans. Electron Devices*, vol. 70, no. 12, pp. 6399–6405, Dec. 2023, doi: 10.1109/TED.2023.3323415.

[17] W.-L. Chang, C.-C. Meng, J.-S. Syu, C.-L. Wang, and G.-W. Huang, "2.4-GHz 7.4-mW 300-kHz flicker-noise-corner direct conversion receiver using 0.18 μm CMOS and deep-n-well NPN BJT," in *2013 IEEE Radio and Wireless Symposium*, Austin, TX, USA: IEEE, Jan. 2013, pp. 223–225. doi: 10.1109/RWS.2013.6486695.

[18] D. Dhar, P. T. M. Van Zeijl, D. Milosevic, H. Gao, and P. G. M. Baltus, "Noise analysis of a BJT-based charge pump for low-noise PLL applications," in *2017 European Conference on Circuit Theory and Design (ECCTD)*, Catania, Italy: IEEE, Sep. 2017, pp. 1–4. doi: 10.1109/ECCTD.2017.8093234.

[19] F. Xi *et al.*, "Tribotronic bipolar junction transistor for mechanical frequency monitoring and use as touch switch," *Microsyst Nanoeng*, vol. 4, no. 1, p. 25, Nov. 2018, doi: 10.1038/s41378-018-0026-1.

[20] G. Wang *et al.*, "Two dimensional materials based photodetectors," *Infrared Physics & Technology*, vol. 88, pp. 149–173, Jan. 2018, doi: 10.1016/j.infrared.2017.11.009.

[21] Z. Xie, Z. Deng, J. Huang, Z. Xie, Z. Zhou, and B. Chen, "InP-Based Extended-Short Wave Infrared Heterojunction Phototransistor," *J. Lightwave Technol.*, vol. 39, no. 14, pp. 4814–4819, Jul. 2021, doi: 10.1109/JLT.2021.3076238.

[22] Qin W., Ma Z., Li H., Zhang L., and Lu B., "Parallel Finite Element Simulations on Radiation Damage Effects of Lateral PNP BJTs," vol. 32, no. 12, 2020, doi: 10.16182/j.issn1004731x.joss.20-FZ0477.

[23] Y. Jiang, W. J. Zhang, J. S. Jie, X. M. Meng, X. Fan, and S.-T. Lee, "Photoresponse Properties of CdSe Single-Nanoribbon Photodetectors," *Adv. Funct. Mater.*, 2007.

[24] P. V. Shinde, A. Tripathi, R. Thapa, and C. Sekhar Rout, "Nanoribbons of 2D materials: A review on emerging trends, recent developments and future perspectives," *Coordination Chemistry Reviews*, vol. 453, p. 214335, Feb. 2022, doi: 10.1016/j.ccr.2021.214335.

[25] J. Jiang *et al.*, "Self-powered photoelectrochemical sensing for sensitive detection of chloramphenicol based on sulfur-vacancy engineered MoS2 nanoribbons/plasmonic Ti3C2 MXene with continual injection of photoinduced electrons," *Journal of Environmental Chemical Engineering*, vol. 12, no. 2, p. 112067, Apr. 2024, doi: 10.1016/j.jece.2024.112067.

[26] H. S. Lee *et al.*, "MoS$_2$ Nanosheet Phototransistors with Thickness-Modulated Optical Energy Gap," *Nano Lett.*, vol. 12, no. 7, pp. 3695–3700, Jul. 2012, doi: 10.1021/nl301485q.

[27] Y. Park, A. J. Hwang, C. Lee, G. Yoo, and J. Heo, "Broadband photodetection of MoS2/p-Ge/n-Ge bipolar heterojunction phototransistor," in *Conference on Lasers and Electro-Optics*, San Jose, California: Optica Publishing Group, 2021, p. STh5B.3. doi: 10.1364/CLEO_SI.2021.STh5B.3.

[28] R. Ghalamboland, S. Darbari, M. Rashidifar, and Y. Abdi, "MoS$_2$/Si-Based Heterojunction Bipolar Transistor as a Broad Band and High Sensitivity Photodetector," *IEEE Sensors J.*, vol. 21, no. 13, pp. 14784–14788, Jul. 2021, doi: 10.1109/JSEN.2021.3074380.

[29] V. Mackowiak, J. Peupelmann, and Y. Ma, "NEP – Noise Equivalent Power".

[30] K. A. Sablon, A. Sergeev, S. Najmaei, and M. Dubey, "High-response hybrid quantum dots- 2D conductor phototransistors: recent progress and perspectives," *Nanophotonics*, vol. 6, no. 6, pp. 1263–1280, Mar. 2017, doi: 10.1515/nanoph-2016-0159.

[31] Z. Wang *et al.*, "Template-Guided C8-BTBT/MAPbBr$_3$/C8-BTBT Heterostructures for Broadband Bipolar Phototransistors," *Adv Materials Inter*, vol. 9, no. 12, p. 2102344, Apr. 2022, doi: 10.1002/admi.202102344.

[32] A. Abderrahmane, C. Woo, and P. J. Ko, "Multifunctional WSe2/SnSe2/WSe2 van der Waals heterostructures," *J Mater Sci: Mater Electron*, vol. 33, no. 15, pp. 11841–11850, May 2022, doi: 10.1007/s10854-022-08147-3.

[33] X. Liu *et al.*, "Transparent, High-Performance Thin-Film Transistors with an InGaZnO/Aligned-SnO$_2$-Nanowire Composite and their Application in Photodetectors," *Advanced Materials*, vol. 26, no. 43, pp. 7399–7404, Nov. 2014, doi: 10.1002/adma.201401732.

[34] S. Guo *et al.*, "Low-Voltage and High-Gain Ultraviolet Detector Based on 4H-SiC n-p-n Bipolar Phototransistor," *IEEE Trans. Electron Devices*, vol. 68, no. 5, pp. 2342–2346, May 2021, doi: 10.1109/TED.2021.3068243.

[35] P. Zhu, P. Zhao, J. Nie, G. Hu, L. Li, and Y. Zhang, "Ultra-high sensitivity strain sensor based on piezotronic bipolar transistor," *Nano Energy*, vol. 50, pp. 744–749, Aug. 2018, doi: 10.1016/j.nanoen.2018.06.035.

[36] Y. Tian *et al.*, "Drive design and performance test of a tunable DFB laser," in *2017 Chinese Automation Congress (CAC)*, Jinan: IEEE, Oct. 2017, pp. 4024–4027. doi: 10.1109/CAC.2017.8243484.

[37] Y. Takezawa, N. Taketani, S. Tanno, and S. Ohara, "Light absorption due to higher harmonics of molecular vibrations in transparent amorphous polymers for plastic optical fibers," *J Polym Sci B Polym Phys*, vol. 30, no. 8, pp. 879–885, Jul. 1992, doi: 10.1002/polb.1992.090300810.

[38] N. Ali, S. A. A. Syed Junid, N. A. M. Ahmad, M. R. Che Beson, and R. Endut, "Identification of C-H Bond Vibration Mode Using Absorption Spectroscopy By A Simple Optically Configured Setup," *JOE*, Jul. 2021, doi: 10.53655/joe.c1987k.